Research Article | Vol. 30, No. 25 / 5 Dec 2022 / Optics Express 45648
Optics EXPRESS

Derivation of uncertainty budgets for continuous above-water radiometric measurements along an Atlantic Meridional Transect

JUNFANG LIN,[1,*] GIORGIO DALL'OLMO,[1,2,3] GAVIN H. TILSTONE,[1] ROBERT J. W. BREWIN,[1,4] VIKTOR VABSON,[5] ILMAR ANSKO,[5] HAYLEY EVERS-KING,[6] TANIA CASAL,[7] AND CRAIG DONLON[7]

[1]*Plymouth Marine Laboratory, Prospect Place, The Hoe, Plymouth, PL1 3DH, UK*
[2]*National Centre for Earth Observation, Plymouth PL1 3DH, UK*
[3]*Istituto Nazionale di Oceanografia e di Geofisica Sperimentale, 34010 Sgonico, Italy*
[4]*Centre for Geography and Environmental Science, College of Life and Environmental Sciences, University of Exeter, Penryn Campus, Penryn TR10 9FE, UK*
[5]*Tartu Observatory, University of Tartu, 61602 Tõravere, Estonia*
[6]*EUMETSAT, Eumetsat Allee 1, 64295 Darmstadt, Germany*
[7]*European Space Agency (ESA) - European Space Research and Technology Centre (ESTEC) Keplerlaan 1, Noordwijk, Netherlands*
[*]*Junl@pml.ac.uk*

Abstract: Fiducial reference measurements are in-situ data traceable to metrology standards, with associated uncertainties. This paper presents the methodology used to derive the uncertainty budget for underway, above-water measurements from the Seabird Hyperspectral Surface Acquisition System deployed on an Atlantic Meridional Transect in 2018. The average uncertainty of remote sensing reflectance for clear sky days was ~ 6% at wavelengths < 490 nm and ~ 12% at wavelengths > 550 nm. The environmental variability such as sun position, wind speed and skylight distribution caused the greatest uncertainty. The different components of the uncertainty budget are critically assessed to indicate how the measurement procedure could be improved through reducing the principal uncertainty sources.

1. Introduction

Satellite ocean colour products are used operationally in many marine applications; from monitoring water quality, to fisheries management and climate risk analysis. The primary data product in satellite ocean colour is remote-sensing reflectance (R_{rs}, sr^{-1}) or normalized water-leaving radiance (nL_w, $mWcm^{-2}\mu m^{-1}sr^{-1}$), which can be inverted to estimate other optical and bio-geochemical variables [1–3]. To ensure these data are of high quality, the ocean-colour R_{rs} product must be validated against coincident *in-situ* radiometric measurements. To facilitate this, the concept of fiducial reference measurements (FRM) was defined for ocean color applications [4] whereby *in-situ* data for satellite validation must comply with the following six key criteria:

(1) Full International System of Units (SI) traceability through regular, documented, calibration and intercomparison.

(2) Independence from the satellite geophysical retrieval process.

(3) An uncertainty budget for all instruments and derived measurements.

#470994 https://doi.org/10.1364/OE.470994
Journal © 2022 Received 27 Jul 2022; revised 8 Oct 2022; accepted 25 Oct 2022; published 1 Dec 2022

Optics EXPRESS

(4) Adhere to community wide and openly published protocols for deployment, measurements, processing, and archiving.

(5) Available for independent verification.

(6) Referenced to inter-comparison exercises.

There is a growing body of work on determining the sources of uncertainty in field radiometric measurements and ways to overcome these through instrument design, deployment methodology, corrections, appropriate data filtering and inter-comparison exercises [4–7]. The validation of satellite radiometric data requires a high number of field measurements with low uncertainties, made across optically diverse water types. Reconciling these two aspects can be difficult in practice, where the opportunities to make measurements are limited (due to cost constraints and accessibility), and ideal conditions (e.g., clear sky, low wind) can be infrequent. These problems have been addressed by deploying autonomous systems on fixed platforms, such as the AERONET-OC network, in which frequent calibration of the instruments and detailed characterization of the instrument uncertainties are routinely undertaken to ensure that under optimal environmental conditions, only the highest quality data are used [8,9]. The AERONET-OC infrastructure is global, but mainly restricted to the coastal zone [8]. To extend radiometric measurements to more remote areas, autonomous sensors have been deployed on research vessels and ships of opportunity [9–14], however the level of data quality deployed on AERONET-OC has not been reproduced for these more unstable platforms.

Underway measurement systems that are deployed quasi autonomously on vessels have the potential to collect vast quantities of data in oceanic areas that are difficult to access and that cover a wide range of optical and environmental conditions. These data are only reliable if their associated uncertainties are quantified. By assessing the uncertainty of ship-borne measurements under such diverse optical conditions, one can potentially increase the number of matchups with satellite overpasses, which enables validation of satellite products in areas that cannot be assessed using fixed platforms [15]. The total uncertainty for these measurements can then be used to select the highest-quality data for validation [16]. This is particularly important to maximise the number of high-quality data points from autonomous systems for match-up analysis, where the uncertainty is likely to vary significantly, particularly if there is rapid environmental change over the duration of the measurements. In turn, uncertainty budgets can be used as a guide to focus on how *in-situ* measurements can be improved, through better instrument characterization and processing of the data in order to reduce uncertainties. Finally, *in-situ* data are frequently used to derive algorithms for estimating biological products from satellite radiometry such as chlorophyll-a (Chl *a,* mg/m^3) concentrations. The uncertainty of these measurements is also required to derive full uncertainty budgets for the associated satellite products. To our knowledge, this is the first time an uncertainty budget has been presented for semi-autonomous radiometric measurements taken on a basin wide field campaign.

The International Organization for Standardization (ISO) Guide to the Expression of Uncertainty in Measurement (GUM) [17] presents the Law of Propagation of Uncertainty (LPU) of expressing uncertainty in measurements and provides a comprehensive approach for estimating the uncertainty [18]. In this study, we describe how to derive the uncertainty budget for underway, above-water radiometric data from the Seabird HyperSAS package using the LPU. We present the uncertainty calculation applied to the radiometric measurements collected on an Atlantic Meridional Transect conducted in 2018 (AMT28). We compute a budget associated with the different uncertainty sources and assess where the uncertainties can be reduced.

Optics EXPRESS

2. Data and Methods

2.1. Study area

The AMT is a multidisciplinary programme that undertakes biological, chemical, physical oceanographic research during an annual voyage between the UK and the South Atlantic. In this study, we characterized the uncertainty budget for continuous above-water radiometric measurements taken over 35 days between 24th September to 28th October during AMT28 on *RRS James Clark Ross*. The transect (>12,000 km) crosses a range of water types from sub-polar to tropical, from euphotic shelf seas and upwelling systems, to oligotrophic mid-ocean gyres, which offers the opportunity to study above-water measurements over a wide range of environmental conditions.

2.2. Data and processing

2.2.1. Instrument installation and radiometric data collection

A SeaBird HyperSAS package was installed on a fixed pole on the bow of the ship (Fig. 1). Hyperspectral downwelling irradiance (E_s, mWcm$^{-2}\mu m^{-1}$), sky radiance (L_i, mWcm$^{-2}\mu m^{-1}$sr^{-1}) and total surface radiance (L_t, mWcm$^{-2}\mu m^{-1}$sr^{-1}) were recorded along the AMT track. The L_t sensor was pointed at the water surface at an angle of 40° from nadir (θ_v), the L_i sensor was at the identical azimuth angle (φ_v) as L_t and pointed to the sky at an angle of 40° from the zenith ($\theta'_v = \theta_v$). The E_s sensor was mounted at the highest point of the ship on the meteorological mast. Measurements were collected during day light hours from ~8 am to ~7 pm at a frequency of ~1 − 5 seconds. The spectral resolution (FWHM) of the radiometers is 10 nm with a spectral step of 3.3 nm and a spectral range from ~ 305 nm to ~ 1142 nm.

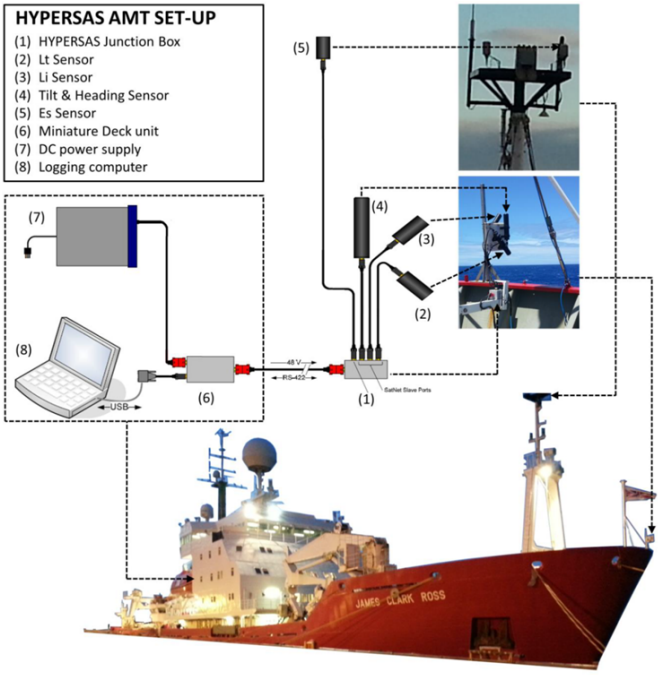

Fig. 1. HyperSAS set-up on *RRS James Clark Ross* for AMT28.

Optics EXPRESS

2.2.2. Auxiliary data

Auxiliary data for processing the HyperSAS data were retrieved from the ship's GPS and meteorological sensors, which include latitude, longitude, time, wind, heading, tilt, pitch, and roll. Wind speed from the ship's anemometer was converted to the true wind speed using the vessel course and speed over water. The solar geometry was calculated as well as the sensor's position to give the relative azimuth angle ($\Delta\varphi$) of the instrument with respect to the sun azimuth. These data were used for data filtering and quality control during data processing. A flowchart of data processing can be found in Fig. 2.

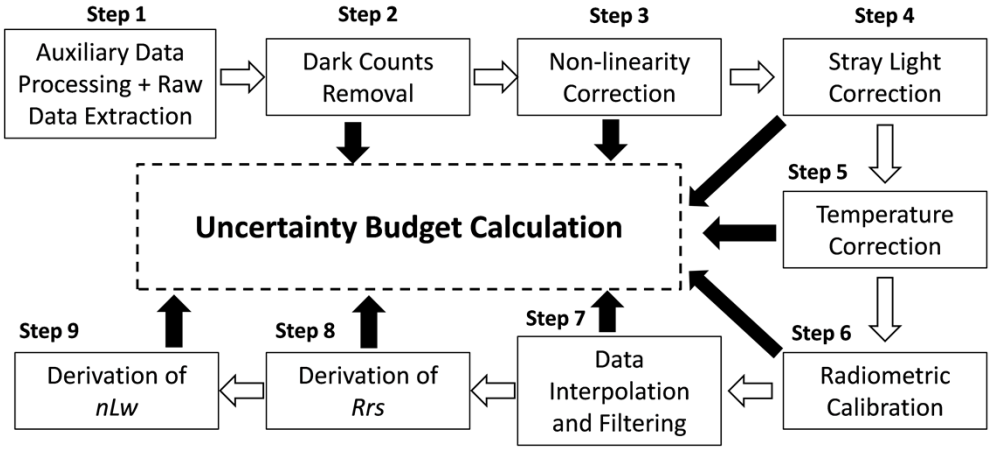

Fig. 2. Flowchart of radiometric data processing on AMT28.

2.2.3. Dark counts

On each instrument a shutter closes periodically (10-minute interval) to record dark counts. Once the raw data were extracted using SatCon (Satlantic's log file data conversion software), the files were merged into single, daily files, combining the measurements from all sensors, associated with the instrument package. The dark value data in time were interpolated to match the light value data for each individual measurements and then subtracted from the raw data of the specific instrument.

2.2.4. Non-linearity correction

The non-linearity characterization of the radiometers was performed at the University of Tartu [19], and the correction factors were calculated following Vabson, et al. [20]. Briefly, non-linearity correction coefficients of the radiometers are determined measuring the radiant exposure from a stable light source (i.e. the calibration source – 1 kW FEL lamp at 500 mm distance) with two to three different integration times. Radiant exposure is the radiant energy received at a surface per unit area which is equivalent to the irradiance of a surface integrated over time of illumination. This is determined during the radiometric calibration. The ratio between the recorded signals (and between integration times) is two to four. For the determination of non-linearity only two different integration times are sufficient.

The non-linearity correction c_{lin} is calculated as

$$c_{lin} = 1 - \delta x = 1 - \alpha \cdot DN, \tag{1}$$

Optics EXPRESS

where δx is relative non-linearity error, α is the non-linearity coefficient, and DN is dark corrected raw value in digital number. The non-linearity coefficient α can be calculated from:

$$\alpha(\lambda) = \frac{\delta x}{DN_{1,2}} = \frac{DN_2 - DN_{1,2}}{{DN_{1,2}}^2}, \tag{2}$$

where $DN_{1,2}$ is the linearity corrected spectrum derived from laboratory measurements and calculated as

$$DN_{1,2} = \left[1 - \left(\frac{DN_2}{DN_1} - 1\right)\left(\frac{1}{t_2/t_1 - 1}\right)\right] DN_1, \tag{3}$$

The spectra DN_1 and DN_2 are measured at different integration times t_1 and t_2 while measuring the same stable radiance/irradiance source. The signal is in dark corrected digital numbers. Relative non-linearity error is calculated as

$$\delta x = \frac{DN_2 - DN_{1,2}}{DN_{1,2}}, \tag{4}$$

A non-linearity correction can then be applied as follows:

$$DN_{corr} = c_{lin} \cdot DN, \tag{5}$$

Or

$$DN_{corr}(\alpha) = (1 - \alpha \cdot DN) \cdot DN \tag{6}$$

The non-linearity correction c_{lin} can also be used with raw data in arbitrary units. Further details of this procedure are given in Zibordi, et al. [21] and Vabson, et al. [20].

2.2.5. Stray light correction

High levels of spectral stray light can lead to significant distortion of the measured signal causing a significant source of uncertainty in the field measurements. A thorough stray light characterisation for radiance and irradiance radiometers was performed at the University of Tartu [19]. A stray-light matrix (SLM) of each spectrometer was determined using a tunable monochromatic laser. These matrixes were applied to raw counts of each $L_t(\lambda)$, $L_i(\lambda)$ and $E_s(\lambda)$ spectra for compensation of stray light effects. More details can be found in Zong, et al. [22] and Ansko, et al. [19].

2.2.6. Temperature correction

Temperature can significantly affect the spectral response of the instrument's silicon photodiodes [23]. The temperature characterisation of each radiance and irradiance sensor was performed at the University of Tartu and used to correct temperature-dependent variability in the radiometric data. To determine the instrument temperature response, the radiometers were immersed into a cylindrical thermally controlled water tank. The water in the tank was circulated by a Julabo FL300 cooler. The tank temperature was measured by a TSYS01 temperature sensor at the outlet port of the tank. A computer automatically controlled the temperature and acquired the spectra. The temperature coefficients and their uncertainties were determined from the temperature and radiometric measurements following Zibordi, et al. [24] and Zibordi, et al. [23]. The dependence on temperature response was corrected from the field spectra as follows:

$$DN_{corr}(T, T_{cal}) = \chi(T, T_{cal}) \cdot DN(T) \tag{7}$$

$$\chi(T, T_{cal}) = 1 - c_T \cdot \Delta T \tag{8}$$

where T(°C) is the radiometer internal temperature recorded by the internal thermal sensor when measurements are taken; T_{cal} is a reference temperature of the radiometric calibration of the spectrometers performed in laboratory conditions at (21 ± 1)°C; DN are raw counts after subtracting the dark count measured at the temperature T; c_T are temperature coefficients; $\Delta T = T - T_{cal}$.

Optics EXPRESS

2.2.7. Radiometric calibration

Radiometric calibration coefficients for each sensor were measured at the University of Tartu following the methods of Vabson, et al. [20]. The average calibration of pre- and post- cruise (calibrated on 20th June, 2018 and 7th March, 2019, respectively) was applied to each instrument. The physical values of each instrument were determined by:

$$X = DN_{corr}^{X} \cdot S_X \tag{9}$$

where DN_{corr}^{X} is the corrected digital number with X representing L_t, L_i or E_s, and S_X is the conversion factor (gain) between physical values and digital numbers.

2.2.8. Data interpolation and filtering

The steps used for the data reduction are as follows:

- Measurement data were interpolated to a common wavelength set (350 to 860 at 2 nm resolution).
- As the three sensors have different integration times and therefore collect data using slightly different time stamps, the E_s, L_i and L_t data were interpolated to the same set of time stamps, which was selected based on the sensor with the slowest integration time (i.e., the L_t instrument).
- Auxiliary data were then also interpolated on to the time stamps of the radiometric instruments.
- The data were then filtered to remove any instances where tilt >5° [11].
- Filtering was also applied to remove data affected by sun glint based on L_t measurements in the near-infrared (NIR) [5]. Specifically, after aggregating the data in 2-minute bins, the spectra corresponding to $L_t(780)$ within the 20th percentile of $L_t(780)$ in each bin were retained.
- Data were discarded that had high solar zenith (>80°) and relative azimuth angles $100<\varphi>170$.
- Any spectra with negative values at 443 nm were removed.

2.2.9. Derivation of R_{rs}

R_{rs} was calculated from the above-water measurements after data interpolation and filtering:

$$R_{rs}(\lambda) = \frac{L_w(\lambda, \theta_v, \varphi_v)}{E_s(\lambda)} \tag{10}$$

$$L_w(\lambda, \theta_v, \varphi_v) = L_t(\lambda, \theta_v, \varphi_v) - \rho(\lambda, \theta_v, \varphi_v) L_i(\lambda, \theta_v', \varphi_v) - \Delta L \tag{11}$$

where L_t, L_i and E_s are the filtered data from the three instruments; L_w ($\mathrm{mWcm^{-2}}\mu m^{-1}\mathrm{sr^{-1}}$) is water-leaving radiance; ρ (dimensionless) is the effective sea-surface reflectance applied to correct for the sun and sky light reflected by the sea surface; the measurement geometry (θ_v, θ_v' and φ_v) was described in section 2.2.1; ΔL ($\mathrm{mWcm^{-2}}\mu m^{-1}\mathrm{sr^{-1}}$) is a spectrally-flat residual term representing radiative contributions due to glint, foam, sea spray and whitecaps. To simplify the notation, the dependence on the viewing geometry and wavelength (λ) can be omitted.

Optics EXPRESS

The values of ρ and ΔL were derived from measurements of L_t and L_i at *NIR* wavelengths using a non-linear optimization technique (Octave *optim* package) that fitted the following equation with the objective of ensuring that the average of measured and estimated $L_t(NIR)$ was minimal:

$$L_t(NIR) = \rho L_i(NIR) - \Delta L \tag{12}$$

with the cost function:

$$Fun = \frac{1}{n}\sum_{i}^{n} |\rho \cdot L_i(\lambda_i) - \Delta L - L_t(\lambda_i)| \tag{13}$$

where λ_i is in the spectral range of *NIR* from 750 nm to 800 nm.

2.2.10. Derivation of nL_w

The water-leaving radiance strongly depends on the type and concentration of the optically significant water constituents and also on viewing and illumination geometries. To normalize for non-nadir views, the approach of Morel, et al. [25] was employed, which uses Chl *a* to estimate the correction for the bidirectional reflectance distribution function. The Chl *a* were estimated from the R_{rs} spectra [26] following:

$$Chla = 10^{a_0+a_1\cdot R+a_2\cdot R^2+a_3\cdot R^3} + a_4 \tag{14}$$

where $R = \log_{10}[R_{rs}(490)/R_{rs}(555)]$ and the coefficients are as follows: $a_0 = 0.319$, $a_1 = -2.336$, $a_2 = 0.879$, $a_3 = -0.135$, and $a_4 = -0.07$ [26]. Further, the radiance L_w corrected for non-nadir view was derived from:

$$L_{w0}(0, 0, \theta_s, \lambda) = L_w(\theta_v, \varphi_v, \theta_s, \lambda) \cdot s_f \tag{15}$$

$$s_f = \frac{\mathfrak{R}(0, w_s)}{\mathfrak{R}(\theta_v, w_s)} \cdot \frac{\frac{f}{Q}(\theta_v, \varphi_v, \theta_s, \lambda, Chla)}{\frac{f}{Q}(0, 0, \theta_s, \lambda, Chla)} \tag{16}$$

where $\mathfrak{R}$ accounts for the sea surface reflectance and refraction as a function of θ_v and wind speed (w_s, m/s); L_{w0} ($\mathrm{mWcm^{-2}}\mu m^{-1}\mathrm{sr^{-1}}$) is exact water-leaving radiance; the f factor relates the ratio of upward to downward sub-surface irradiance to the total water absorption and backscattering; Q is the ratio between subsurface upward irradiance and water-leaving radiance; the values of $\mathfrak{R}$ and $\frac{f}{Q}$ were taken from the lookup table of Morel, et al. [25].

The exact normalized leaving radiance (nL_w) is further calculated according to:

$$nL_w = \frac{L_{w0} \cdot F_0}{E_s} \tag{17}$$

where F_0 ($\mathrm{mWcm^{-2}}\mu m^{-1}$) is the solar irradiance at the top of the atmosphere at the mean Sun-Earth distance and its values were taken from Thuillier, et al. [27]. A Sun-Earth distance correction was also conducted to correct local deviations. Combining Eq. (10) with the above equation we obtain:

$$nL_w = R_{rs} \cdot s_f \cdot F_0 \tag{18}$$

2.3. Calculation of uncertainty

2.3.1. Law of propagation of uncertainty for R_{rs}

The uncertainty budget for the above-water radiometers follows the methodology defined by the LPU [17]. The combined variance for the uncertainty associated with R_{rs} was calculated as

Optics EXPRESS

follows:

$$\mu_{R_{rs}}^2 = \left(\frac{\partial R_{rs}}{\partial L_t}\mu_{L_t}\right)^2 + \left(\frac{\partial R_{rs}}{\partial L_i}\mu_{L_i}\right)^2 + \left(\frac{\partial R_{rs}}{\partial E_S}\mu_{E_s}\right)^2 + \left(\frac{\partial R_{rs}}{\partial \rho}\mu_{\rho}\right)^2 + \left(\frac{\partial R_{rs}}{\partial \Delta L}\mu_{\Delta L}\right)^2 + 2\sum_i \sum_j \frac{\partial R_{rs}}{\partial x_i}\frac{\partial R_{rs}}{\partial x_j}\mu_{x_i}\mu_{x_j} r(x_i, x_j) \tag{19}$$

where μ is the uncertainty associated with each variable (R_{rs}, L_t, L_i, E_s, ρ and ΔL) in its physical unit; the partial derivative terms are the sensitivity coefficients with respect to each source of uncertainty; and the second line of equation (Eq. (19)) takes into account correlations (r) between each of these components (x, $i \neq j$). Each sensitivity coefficient in Eq. (19) can be further expressed as:

$$\frac{\partial R_{rs}}{\partial L_t} = \frac{1}{E_s} \tag{20}$$

$$\frac{\partial R_{rs}}{\partial L_i} = -\frac{\rho}{E_s} \tag{21}$$

$$\frac{\partial R_{rs}}{\partial_{E_s}} = \frac{-L_t + \rho L_i + \Delta L}{(E_s)^2} \tag{22}$$

$$\frac{\partial R_{rs}}{\partial \rho} = \frac{-L_i}{E_s} \tag{23}$$

$$\frac{\partial R_{rs}}{\partial \Delta L} = -\frac{1}{E_s} \tag{24}$$

For a full description of the uncertainty propagation of L_t, L_i and E_s, the starting point is the conversion between digital numbers to physical values associated with radiometric calibration. An example of this procedure for L_t is given as:

$$L_t = (DN_{L_t} - DK_{L_t})S_{L_t} \tag{25}$$

where DN_{Lt} is the digital number for L_t, DK_{Lt} is the dark signal in counts (dark counts), and S_{Lt} is the conversion factor. The uncertainty of L_t can then be derived using:

$$\mu_{L_t}^2 = \left(\frac{\partial L_t}{\partial DN_{L_t}}\mu_{DN_{L_t}}\right)^2 + \left(\frac{\partial L_t}{\partial DK_{L_t}}\mu_{DK_{L_t}}\right)^2 + \left(\frac{\partial L_t}{\partial S_{L_t}}\mu_{S_{L_t}}\right)^2 \tag{26}$$

The partial terms in Eq. (26) can be derived as

$$\frac{\partial L_t}{\partial_{DN_{L_t}}} = S_{L_t} \tag{27}$$

$$\frac{\partial L_t}{\partial_{DK_{L_t}}} = -S_{L_t} \tag{28}$$

$$\frac{\partial L_t}{\partial_{S_{L_t}}} = DN_{L_t} - DK_{L_t} \tag{29}$$

The uncertainty of measurement counts ($\mu_{DN_{L_t}}$) was determined by the standard deviation of the raw data from each instrument within each 2 minutes chunk. For the uncertainty of dark counts ($\mu_{DK_{L_t}}$), it was calculated from three dark measurements in a row within 30 minutes. The uncertainty of the gain factor ($\mu_{S_{L_t}}$) consisted of two separate components: inherent uncertainty during the calibration procedure and sensor drift with time. For calibration, the inherent uncertainties in percentage are ~2.4% for radiance sensors and ~1.8% for irradiance sensor based

Optics EXPRESS

on repeat measurements made at the calibration facility, and consistent with estimates in the literature [28]. The uncertainty of the sensor drift was calculated as

$$\mu_{drift} = \frac{|S_{L_t}^{post} - S_{L_t}^{pre}|}{\sqrt{12}} \tag{30}$$

It is assumed that the gain factor during the cruise varied between those at the pre- and post-cruise calibrations and the probability density function is a uniform distribution [17,29].

Additional sources of uncertainty (μ_{other}^2) are also considered and added to Eq. (26), so that the final equation for calculating the uncertainty of L_t can be rewritten as:

$$\mu_{L_t}^2 = \left(\frac{\partial L_t}{\partial DN_{L_t}}\mu_{DN_{L_t}}\right)^2 + \left(\frac{\partial L_t}{\partial DK_{L_t}}\mu_{DK_{L_t}}\right)^2 + \left(\frac{\partial L_t}{\partial S_{L_t}}\mu_{S_{L_t}}\right)^2 + \mu_{other}^2 \tag{31}$$

The additional sources of uncertainty were associated with Type B evaluation of standard uncertainty, since some of the parameters used are based on manufacturer specifications and published literature. These factors are probably not constant over time, or spectrally invariant, but in the absence of specific data on this variability, mean literature values were used. For these uncertainties, if the coverage factor (k) isn't provided, a values of $k = 2$ will be used, corresponding to a level of 95% confidence. Furthermore, these sources of Type B uncertainty evaluation were considered independent of each other ($r = 0$). These additional sources of uncertainty are detailed in the following sections and also listed in Table 1.

Table 1. Uncertainties estimated from literature recommendations or laboratory measurements

Sources	Sensor	Uncertainty ($k = 2$)			References
		410 nm	490 nm	550 nm	
non-linearity correction coefficient (α)	E_s	2.25e-7 DN^{-1}	5.32e-8 DN^{-1}	3.27e-8 DN^{-1}	-
	L_t	1.32e-7 DN^{-1}	5.07e-8 DN^{-1}	3.14e-8 DN^{-1}	
	L_i	1.81e-7 DN^{-1}	5.58e-8 DN^{-1}	2.32e-8 DN^{-1}	
C_T	E_s	3.44e-2 $°C^{-1}$	3.19e-2 $°C^{-1}$	3.15e-2 $°C^{-1}$	-
	L_t	3.12e-2 $°C^{-1}$	2.76e-2 $°C^{-1}$	2.69e-2 $°C^{-1}$	
	L_i	2.85e-2 $°C^{-1}$	2.49e-2 $°C^{-1}$	2.41e-2 $°C^{-1}$	
T_{cal}	-	1°C			-
Inherent gain factor (S in Eq.25)	E_s	1.8%			-
	L_i/L_t	2.4%			
straylight correction	E_s/L_i	0.25%			[31]
	L_t	0.5%			
non-cosine response	E_s	2%			[7,31]
	L_i/L_t	0%			
polarization	E_s	0.6%			[7,32]
	L_i/L_t	1.3%			
$\bar{u}_r$	-	50%			[33]
F_0	-	2.5%			[27]

2.3.2. Uncertainty associated with temperature characterization

Following Eq. (7), the uncertainty due to temperature calibration can be calculated from:

$$\mu_{DN_{corr}(T,T_{cal})}^2 = \left(\frac{\partial_{DN_{corr}(T,T_{cal})}}{\partial_{T_{cal}}}\mu_{T_{cal}}\right)^2 + \left(\frac{\partial_{DN_{corr}(T,T_{cal})}}{\partial_{c_T}}\mu_{c_T}\right)^2 \tag{32}$$

Optics EXPRESS

The temperature coefficient (C_T) and its uncertainty (μ_{C_T}) were determined at the University of Tartu [30]. The uncertainty of T_{cal} and C_T are listed in Table 1. The final uncertainty due to the temperature calibration for each measurement (E_s, L_i, and L_t) was calculated using Eq. (25) by replacing $DN_{L_t} - DK_{L_t}$ with $DN_{corr}(T, T_{cal})$.

2.3.3. Uncertainty from non-linearity correction

Similarly, the uncertainty from non-linearity correction was calculated from Eq. (6)

$$\mu^2_{DN_{corr}(\alpha)} = \left(\frac{\partial_{DN_{corr}(\alpha)}}{\partial_\alpha}\mu_\alpha\right)^2 \tag{33}$$

The uncertainty of α for each radiometer (see Table 1) was computed from the standard deviation of the spectra DN_1 and DN_2 measured at different integration times t_1 and t_2 (Eq. (3)) while measuring the same stable radiance/irradiance source.

2.3.4. Uncertainty associated with stray light correction, cosine-response and polarization

The uncertainty associated with stray light correction, cosine-response and polarization were estimated according to literature recommendations [7,31,32]. For straylight correction, the averaged percent uncertainty is 0.025% for E_s and L_i and 0.5% for L_t. There are no uncertainties from non-cosine response for radiance sensors, but 2% for irradiance sensor. For polarization, it is 0.6% for E_s and 1.3% for L_i and L_t. More details are also shown in Table 1.

2.3.5. Uncertainty from the environmental variability

An important aspect of the uncertainty that must be estimated accurately arises from the environmental variability, i.e., temporal and spatial fluctuations associated with variations in illumination and sea surface conditions [34]. For L_t, L_i, and E_s, the uncertainty related to environmental variability was estimated from the standard deviation of the data within 2-minute bins, after the filtering process described above. Similarly, the uncertainty of effective reflectance factor (μ_ρ) and residual term ($\mu_{\Delta L}$) due to environmental variability, were also calculated during 2-minute bins from their respective standard deviations.

2.3.6. Law of uncertainty propagation for nL_w

According to Eq. (18), the uncertainty of nL_w is given by:

$$\mu^2_{nL_w} = \left(\frac{\partial nL_w}{\partial R_{rs}}\mu_{R_{rs}}\right)^2 + \left(\frac{\partial nL_w}{\partial s_f}\mu_{s_f}\right)^2 + \left(\frac{\partial nL_w}{\partial F_0}\mu_{F_0}\right)^2 \tag{34}$$

with partial terms derived as

$$\frac{\partial nL_w}{\partial R_{rs}} = s_f \cdot F_0 \tag{35}$$

$$\frac{\partial nL_w}{\partial s_f} = R_{rs} \cdot F_0 \tag{36}$$

$$\frac{\partial nL_w}{\partial F_0} = R_{rs} \cdot s_f \tag{37}$$

The first term on the right side of Eq. (34) can be directly calculated from S_f, F_0, and $\mu_{R_{rs}}$ with the value of $\mu_{R_{rs}}$ estimated from Eq. (19). For the second term, the value of μ_{s_f} can be estimated according to the finding of Talone, et al. [33], using:

$$\mu_{s_f} = \bar{u}_r \cdot \left(\frac{L_{w_0} - L_w}{L_w}\right) \tag{38}$$

where $\bar{u}_r$ is the uncertainty of non-nadir correction defined in Eq. (15) of Talone, et al. [33] which varies with wavelength and water type, with values of approximately 55% at 412 nm, 20 –

Optics EXPRESS

40% between 490 nm and 551 nm, and exceeding 60% at 667 nm [33]. In this study, an averaged value (50%) is used for all above-water measurements made during AMT28. For the uncertainty of F_0 (μ_{F_0}), a mean relative uncertainty of 2.5% was used [27].

2.4. Clear-sky Detection

To understand the impact of sky illumination on the uncertainty of R_{rs} and nL_w, a clear-sky detection algorithm was used based on Reno and Hansen [35]. In this study, the spectral solar irradiance model of Gregg and Carder [36] for cloudless maritime atmospheres was employed to provide data at the same frequency as the irradiance acquisitions. This spectral irradiance model was used as a reference and interpolated to the same sun angle measurements made over the course of the day. Criteria were designed to screen clouds based on time series of E_s at 550 nm ($E_s(550)$) and are listed in Table 2. Before these criteria were applied, the measurements of $E_s(550)$ were first interpolated into a time series with a constant time interval of 5 sec. Then an optimization procedure was conducted to minimize the following cost function:

$$f = \frac{1}{n}\sqrt{\sum (m(t) - \beta \cdot r(t))^2} \tag{39}$$

where m and r indicate clear-sky measurement and reference, respectively; β is the scaling factor to adjust the magnitude of modeled $E_s(550)$ curve with time; n is the number of clear-sky measurements during the day; and the clear-sky measurements are detected following the criteria in Table 2 with an initial guess of β as 1. After that, a new value of β is obtained from this optimization procedure, which is then used to detect a new set of clear-sky measurements. These steps were repeated until the variation of Eq. (39) in the latest two iterations was <2%. The final clear-sky measurements were determined from the last β according to the criteria in Table 2.

Table 2. Criterions of clear-sky detection algorithm[a]

Name	*Equation*	*Definition*	*Criterion*
Mean difference	$\lvert\bar{v}_m - \beta \cdot \bar{v}_r\rvert$	Absolute difference of mean values in a chunk (75 sec)	<8 μWcm^{-2}nm^{-1}
Minima difference	$\lvert v_m - \beta \cdot v_r\rvert$	Absolute difference of minimal values in a chunk (75 sec)	<8 μWcm^{-2}nm^{-1}
Maxima difference	$\lvert v_m - \beta \cdot v_r\rvert$	Absolute difference of maximal values in a chunk (75 sec)	<8 μWcm^{-2}nm^{-1}
CV difference	$\lvert CV_m - CV_r\rvert$	Absolute difference of CV in a chunk (75 sec)	<2%
Mean distance to reference	$\lvert\bar{v}_m - \bar{v}_r\rvert$	Mean distance to reference in a chunk (75 sec)	<12 μWcm^{-2}nm^{-1}

[a]Subscript m and r indicate measurement and reference (model value), respectively; β is the scale factor derived from optimization by minimizing the cost function of Eq. (39); CV is the coefficient of variation defined as the ratio of standard deviation to mean value.

2.5. Stepwise Regression Analysis

The environmental variability (e.g., sky condition, sun zenith, wind speed) has a big impact on the estimates of R_{rs} (or nL_w). To investigate the significance of each independent variable on the final estimates, a stepwise regression was deployed using a python package (https://www.statsmodels.org/stable/index.html). The backward elimination method was applied, which begins with a full model loaded with all variables and then removes one variable to test its importance relative to the overall results.

Optics EXPRESS

3. Results

3.1. Above-water radiometric measurements

3.1.1. Overview of radiometric measurements on AMT28

The spectral shape and magnitude of R_{rs} and nL_w for the typical Atlantic waters sampled on AMT28 are given in Fig. 3. Only measurements with uncertainties smaller than 10% are shown. The spectra were divided into two types, representative of blue and green waters using the scoring system and water classification method of Wei, et al. [37]. The reference system includes R_{rs} spectra ranging from purple, blue to yellow waters. The scoring system compares R_{rs} spectrum against a reference and gives it a score of between 0 and 1 to indicate unusable and perfect R_{rs} spectrum, respectively. The quality scores for all spectra were high with a value of ~1 (95% spectra had a score of 1), indicating very high quality of R_{rs}. The spectral shape and magnitude of R_{rs} were also consistent with previous studies of Tilstone, et al. [14] and Brewin, et al. [11].

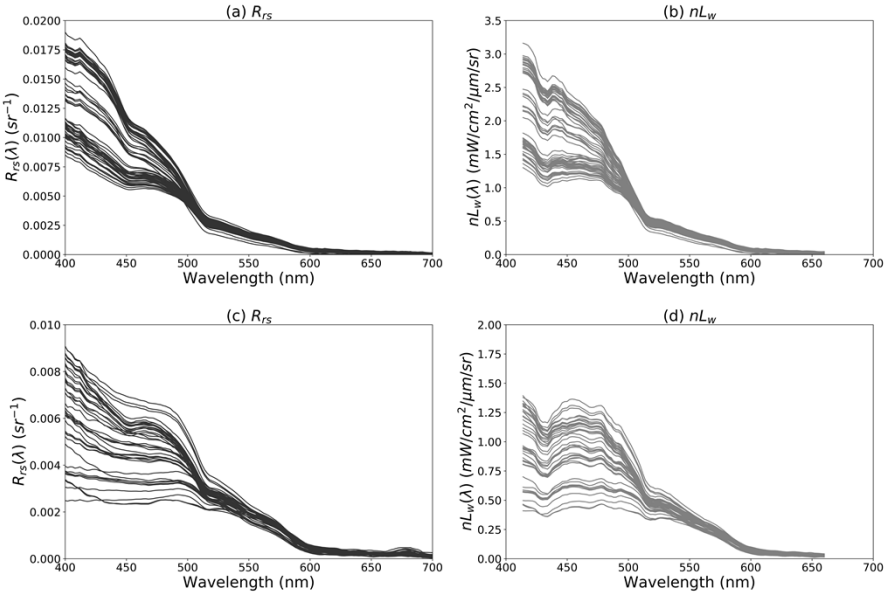

Fig. 3. Spectral shape and magnitude of R_{rs} and nL_w for measurements with uncertainty <10% (as examples of the highest quality measurements that we have that are typical for AMT); (a) and (b) were collected from blue waters, (c) and (d) were collected from green waters.

3.1.2. Distribution of ρ and ΔL

To estimate R_{rs}, skylight was removed from L_t with optimized ρ and ΔL (see Eq. (11)). Figure 4 shows the distribution of ρ and ΔL during AMT28. For all measurements, ρ varied over a wide range from 0.02 to 0.3 with a mean value of ~0.03. In the study of Mobley, et al. [38], a spectral constant ρ (0.028) was suggested for skylight correction under perfect measuring conditions (clear sky, low wind speed) and with a fixed viewing geometry (40°, 135°). For a moving platform however, it can be very challenging to take measurements under such perfect conditions, thus it is questionable whether to use a constant ρ for all measurements. In this study, we observed that ~10% of data had ρ values higher than 0.1 due to a significant effect of surface-reflected light or sun glint (Fig. 4(a)).

To further demonstrate the impact of environmental factors, radiometric measurements were presented for clear sky and cloudy days (Fig. 5). Figure 5(a) shows that for an example clear-sky

Optics EXPRESS

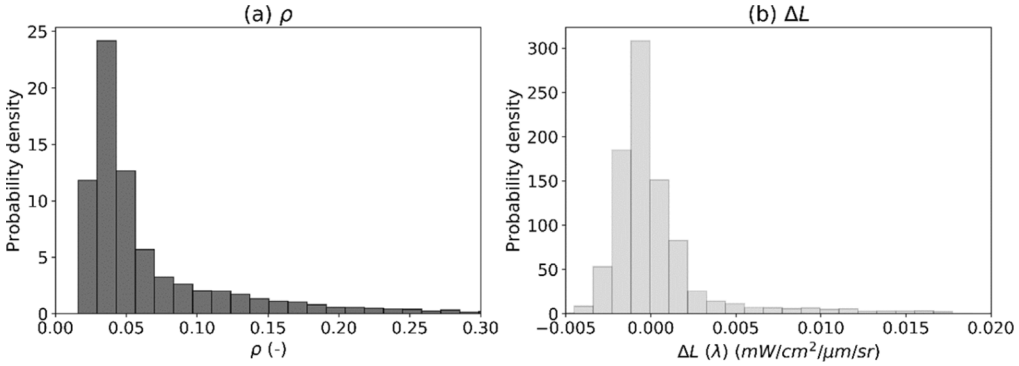

Fig. 4. Histogram distribution of (a) ρ and (b) ΔL for whole cruise.

day, ρ varied over a wide range (~0.02–0.38) with higher values at noon when the solar zenith angle was low. This was due to the significant effects of sun glint on the radiance measurements at lower solar zenith angles during the clear sky conditions. In contrast, the ρ on the cloudy day was more stable (e.g., a constant ρ ~0.03, Fig. 5(b)). ΔL generally were close to zero when solar zenith angle was high for both clear sky and cloudy days, but tended to be positive at noon for the clear sky day (Fig. 5(a)) and to be negative at noon for the cloudy day (Fig. 5(b)).

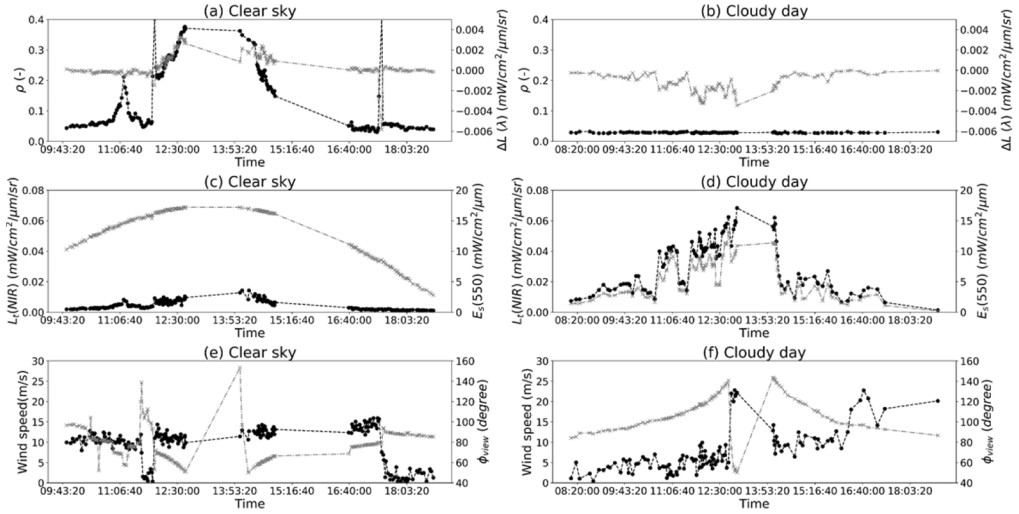

Fig. 5. Time series of (a) ρ, (c) ΔL, $L_t(NIR)$ and $E_s(550)$, (e) wind speed and φ_{view} for clear sky and (b) ρ, (d) ΔL, $L_t(NIR)$ and $E_s(550)$, (f) wind speed and φ_{view} for cloudy sky conditions (left and right axes correspond to black and grey plots, respectively).

3.1.3. Effect of BRDF correction

The impact of the BRDF correction was significant, as indicated by the ratio of L_{w0} to L_w for the entire cruise (Fig. 6). For selected wavelengths (440–660 nm), the ratio ranged from 0.8 to 1.08 with a mean value of ~0.96. These results illustrate that it is critical to apply a BRDF correction to compare data from different platforms with different solar and sensor geometries [33].

Optics EXPRESS

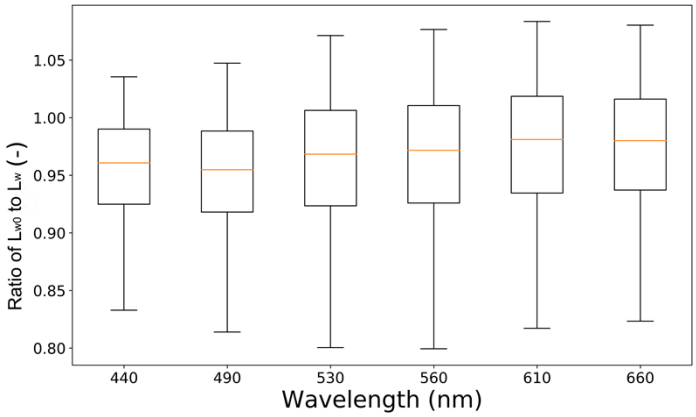

Fig. 6. Ratio of L_{w0} to L_w for whole cruise showing the impact of the BRDF correction. The box extends from the lower to upper quartile values of the ratios, with an orange line as the median. The whiskers extend from the box to show the range of the ratios.

3.1.4. Effects of temperature, straylight and non-linearity correction

Since the temperature, straylight and non-linearity can also impact the radiometric measurements, we investigated their effects by including and excluding these corrections when processing the data. For nL_w the overall absolute difference (ξ) between quantities with and without these corrections was less than ~ 4%, with most of data points less than 2%. ξ was calculated with the following equation:

$$\xi = \left| \frac{x_{cor} - x_{uncor}}{x_{cor}} \right| \cdot 100\% \tag{40}$$

where x_{cor} and x_{uncor} indicate corrected and uncorrected quantities, respectively. A further investigation on the impact of the same corrections on E_s, L_t and L_i is also shown in Fig. 7. The impact of the corrections on E_s were higher compared to the impacts on L_t and L_i which varied from 0 to ~ 2.5% and had a higher impact at longer wavelengths (550 nm, see Fig. 7(f)). The overall impact on L_t and L_i including 550 nm, was slightly lower (0–0.5% and 0–1.0% for L_t and L_i, respectively). The pattern of distribution could be due to the non-normal distribution of environmental variabilities that were related to the corrections.

3.2. Uncertainty of R_{rs} and nLw

3.2.1. Overview of the uncertainty of R_{rs} and *nLw* during AMT28

The variability in percentage uncertainty in R_{rs} ($\mu_{Rrs(\%)}$) during AMT28 varied by both latitude and wavelength (Fig. 8 (a-c)). At 410 nm, $\mu_{Rrs(\%)}$ was generally less than ~100% with 80% of $\mu_{Rrs(\%)}$ in the range of ~2% – 20%. Over the entire AMT28, the average uncertainty of $R_{rs}(410)$ was ~9%. There was a similar distribution for $\mu_{Rrs(\%)}$ at 490 nm (Fig. 8(b)) with a mean of ~10%. For $\mu_{Rrs(\%)}$ at 550 nm (Fig. 8(c)), the percentage uncertainty increased by 5% due to the lower R_{rs}values. Similar results were obtained for the percentage uncertainty of nL_w ($\mu_{nLw(\%)}$), but with an overall increase of 1–2% due to the additional uncertainties arising from the BRDF correction (Fig. 8 (d-f)).

3.2.2. Daily example of the estimation of uncertainty

To investigate in more detail the daily variability in μ_{Rrs}, an in-depth analysis of the uncertainty during clear-sky conditions on 15th October 2018, was conducted. The clear sky conditions were verified using the clear-sky detection algorithm, which showed that ~80% of the measurements

Optics EXPRESS

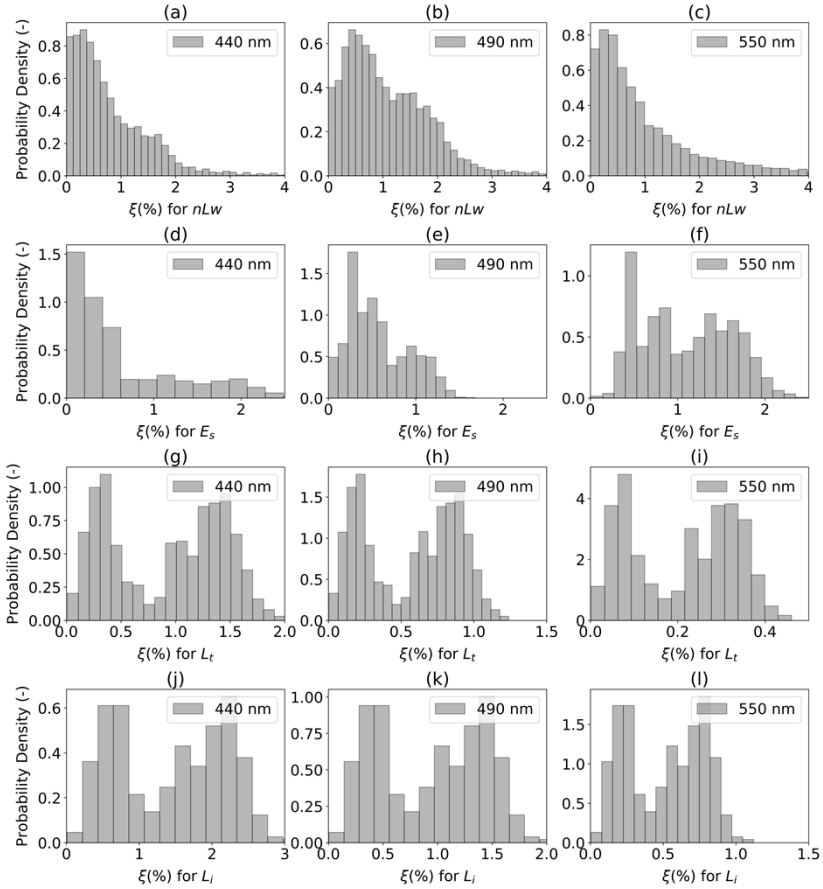

Fig. 7. Distribution of differences between radiometric quantities processed with and without temperature correction, straylight correction, and non-linearity correction: nL_w (a-c), E_s(d-f), L_t(g-i) and L_i(j-l).

were made under clear skies (Fig. S1 in Supplement 1). To avoid other additional errors, data were excluded when the solar zenith was high (> 80° data after 7 pm; Fig. S1a). Estimates of $\mu_{Rrs(\%)}$ between 1 and 4 pm were filtered out because the azimuth angles of the L_t sensor during this period were <80°. The wind speed during 15th October varied from 0.5 to 16 m/s with a mean value of ~10 m/s. At 410 and 490 nm, $\mu_{Rrs(\%)}$ was generally <10% with a mean value of 6%, whereas at 550 nm $\mu_{Rrs(\%)}$ increased ~2 fold due to the decrease in R_{rs} (Fig. 9(a)). The pattern in $\mu_{nLw(\%)}$ was similar (Fig. 9(b)).

By comparison, example measurements for a cloudy day (16th October, 2018; Fig. S1b) and the associated time series of $\mu_{Rrs(\%)}$ and $\mu_{nLw(\%)}$ illustrated that the uncertainties were higher and increased by ~20% (Fig. S2 in Supplement 1).

3.2.3. Contribution to the uncertainty by different components

To understand the uncertainty budget of R_{rs} during AMT28, individual components of the overall uncertainty budget during clear and cloudy days were investigated in more detail. The

Optics EXPRESS

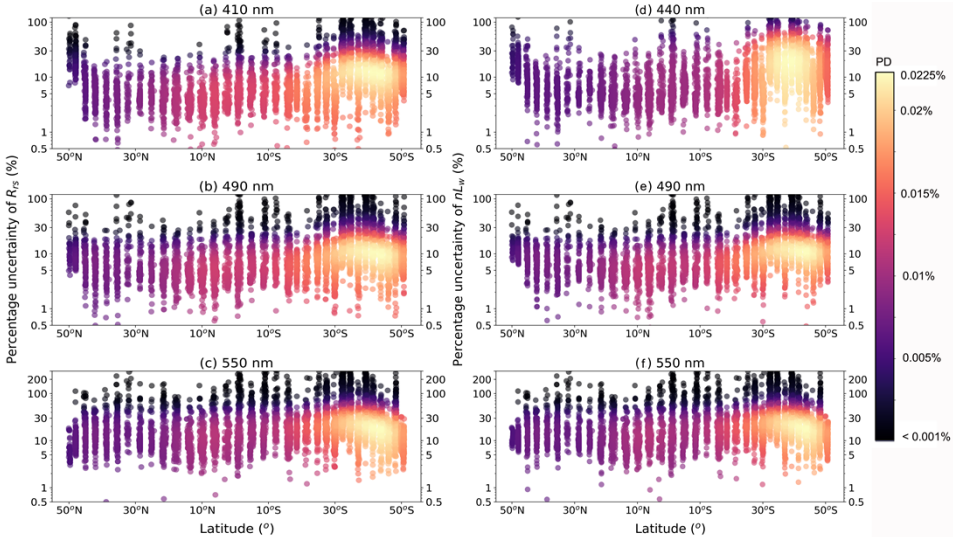

Fig. 8. Percentage uncertainty distribution (%) of R_{rs} and nL_w along the AMT28 campaign track at (a, d) 440, (b, e) 490, (c, f) 550 nm. The colours indicate the probability density (PD) estimated by a Kernel density function (high density in yellow, low density in black). The uncertainty of nL_w at 440 was analyzed instead of 410 nm, because of no non-nadir correction coefficients are available for 410 nm from the look-up table of Morel et.al [25].

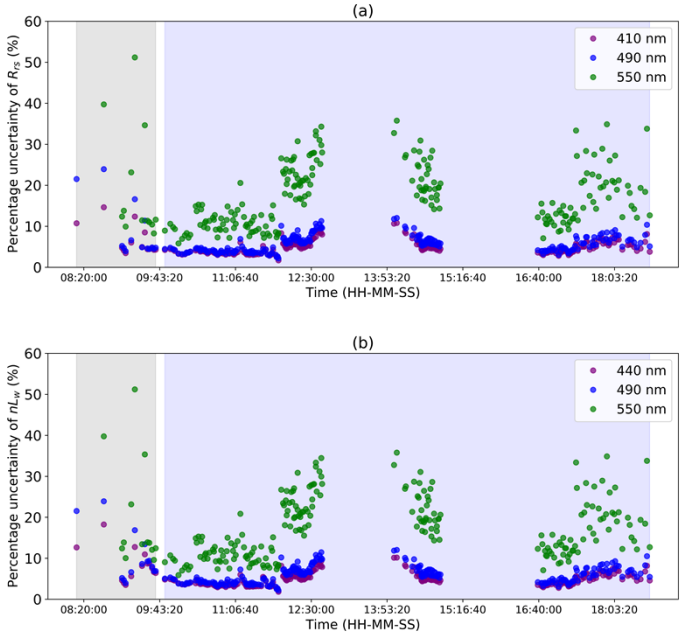

Fig. 9. An example of total percent uncertainty in R_{rs} and nL_w at selected wavelengths on a clear-sky day (15th October 2018). Grey and blue shadows indicate measurements taken under cloudy (grey) and clear-sky (blue) conditions, respectively.

Optics EXPRESS

contribution to the variance in R_{rs} was calculated as:

$$\varsigma_i = \frac{\left(\frac{\partial R_{rs}}{\partial x_i}\mu_{x_i}\right)^2}{{\mu_{R_{rs}}}^2} \cdot 100\% \tag{41}$$

or

$$\varsigma_{ij} = \frac{2\frac{\partial R_{rs}}{\partial x_i}\frac{\partial R_{rs}}{\partial x_j}\mu_{x_i}\mu_{x_j}r(x_i,x_j)}{{\mu_{R_{rs}}}^2} \cdot 100\% \tag{42}$$

where x_i represents each component (L_t, L_i, E_s, ρ and ΔL) shown in Eq. (19).

Figure 10 and Fig. S3 (see Supplement 1) present the contributions of different uncertainty components and correlation terms for clear-sky measurements and cloudy-sky measurements, respectively. Note that only absolute values >1% were shown and for convenience, all other components with values <1% were represented using a summing term.

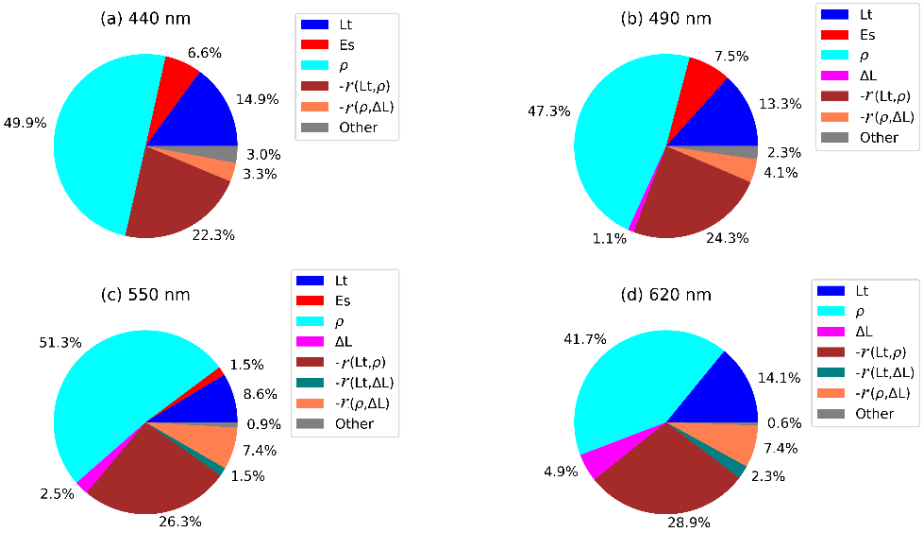

Fig. 10. Contribution of different components of the uncertainty and correlation terms for clear-sky measurements to the overall uncertainty of R_{rs} for the whole cruise (only values >1% are shown); grey colour indicates a sum of other terms with a value <1%.

For clear-sky measurements, the components that contributed most to the uncertainty were ρ and L_t. At 410, 490, 550, 620 nm, ρ had the largest contribution (up to ~ 50%), and the additive contribution of L_t and ρ was ~ 60% (Fig. 10). The correlation between L_t and ρ was negative and contributed significantly to the overall uncertainty (from −22% to −28%). This result suggests that by accounting for this correlation, the overall uncertainty in R_{rs} will be reduced.

For cloudy-sky measurements, L_t and ρ were still the main uncertainty components, with an additive contribution > 50% and a negative correlation contribution of − 25% (Fig. S3). The contribution of L_i was larger than under clear-sky conditions however and generally increased with wavelength (~10% for long wavelengths). This higher uncertainty associated with L_i was mainly due to the inconsistent distribution of sky radiance from clouds.

3.2.4. Assessment of sources of uncertainty that comprise the total budget

The mean contribution of different uncertainty sources to the total uncertainty of L_t during the clear-sky measurements for the whole cruise are given in Fig. 11. The calculation of the contribution of each was similar to Eq. (41). The results showed that the environmental variability

Optics EXPRESS

was the largest source of uncertainty at all wavelengths and accounted for up to 80% of the budget (Fig. 11). Polarization also had a relatively large impact at 410 and 490 nm, but decreased at 550 and 620 nm. The contribution of dark counts increased with wavelength as a result of the lower magnitude of L_t at longer wavelengths. The impact of the uncertainty due to temperature correction was negligible. For comparison, the contribution to the uncertainty budget of the environmental variation during cloudy-sky conditions are shown in Fig. S4 (see Supplement 1) and had a higher (~86%) contribution compared to the clear-sky example (Fig. 10).

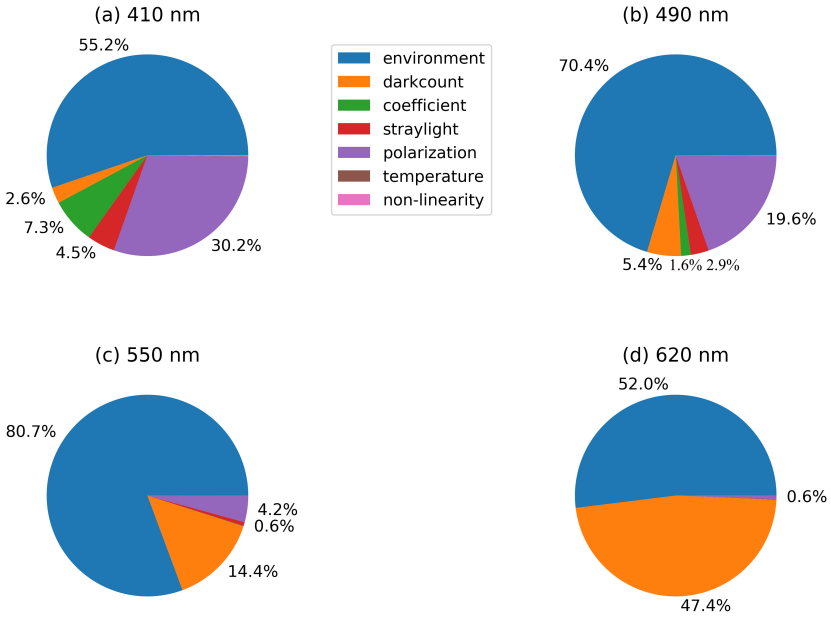

Fig. 11. Uncertainty budget for L_t under clear-sky conditions at (a) 410, (b) 490, (c) 550 and (d) 620 nm.

Similarly, the contribution of each uncertainty source to the total uncertainty in L_i was also investigated (not shown). For clear-sky conditions, the uncertainty in L_i was relatively small, thus the impact of the environmental term was lower than that for L_t, although this contribution still reached ~50% at 620 nm. There was also a relatively high contribution from the uncertainty in polarization at selected wavelengths (up to ~50%). For cloudy skies, the environmental term had the most important contribution to the uncertainty of L_i (> 90%).

For E_s in clear-sky conditions, the contribution of non-cosine response was the most significant with a consistent contribution of ~65% over all wavelengths (data not shown). The contributions of dark count and temperature were very small (<1%). For cloudy days, the environmental term and non-cosine response contributed ~80% and ~15% over the total uncertainty of E_s.

3.3. *Impact of environmental conditions on estimates of R_{rs}.*

During AMT28 radiometric measurements were collected over a wide range of environmental conditions that included clear and cloudy skies, low to high sun zenith angles, low to high wind speeds. This provides an opportunity to investigate how specific environmental factors affect R_{rs}

Optics EXPRESS

(or nL_w). Since ρ and L_t(NIR) make a significant contribution to the uncertainty of R_{rs} (or nL_w), we therefore investigated how the environmental conditions during AMT28 affect ρ and L_t(NIR).

Figure 12 shows the dependency of ρ and L_t(NIR) on the major environmental factors for the radiometric measurements collected on clear-sky days during AMT28. ρ and L_t(NIR) generally decreased with increasing sun zenith (Fig. 12 a, e). For L_t(NIR), the trend is basically consistent with the decreasing surface irradiance with sun zenith (Fig. 12 e). Large ρ values (up to ~ 0.5) were found at low sun zenith angles (Fig. 12 a), consistent with the large ρ values at low φ_v (< 100°, see Fig. 12 b). In this viewing geometry, the radiometric measurements could inevitably be affected by the ambiguous and unpredictable sun glint because of surface waves. An increasing trend between ρ (or L_t(NIR)) and wind speed was observed, indicating that a relative larger amount of glint could be acquired at high wind speeds (Fig. 12 c, g). For wind direction, ρ or L_t(NIR) was slightly higher at wind directions < 100° (Fig. 12 d, h).

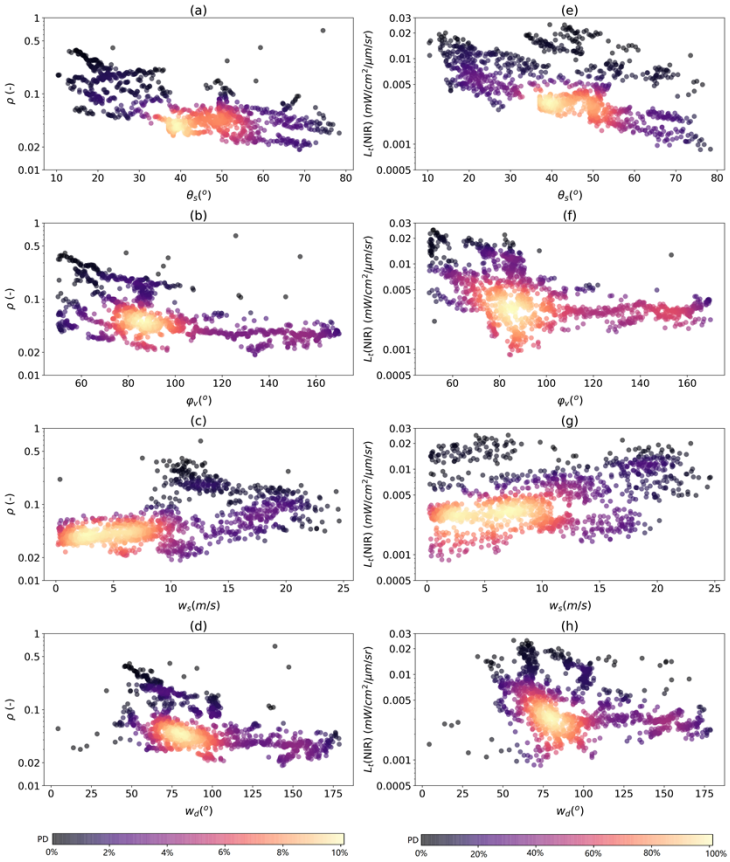

Fig. 12. Dependency of ρ on (a) solar zenith angle, θ_s, (b) relative azimuth angle φ_s, (c) wind speed w_s and (d) wind direction w_d (with respect to the Sun) for clear sky days. Right panel shows similar results but for L_t(*NIR*).

To examine the significance of each independent variable on ρ, a stepwise regression (see Method 2.5) was performed. Table 3 lists the statistics of the linear model between the decimal logarithm of ρ (log(ρ)) and these variables, where the p-values are small and the r^2 is ~ 0.67. By deleting each variable at each level, it allows us to see whether the contribution from each variable is statistically significant (Table 4). It was found that after removing θ_s from the model, r^2 decreased significantly (from 0.67 to 0.45). For other variables, the changes were similar but

Optics EXPRESS

with slightly higher significance for w_s. These results demonstrate that θ_s was the most important factor affecting the variation in ρ.

Table 3. Statistics of a linear model between ρ and major environmental factors[a]

	coefficients	*Std error*	*t*	*P value*
θ_s	-0.0094	0	-29.4	0
φ_v	-0.0013	0	-3.8	0
w_d	-0.0022	0	-7.2	0
w_s	0.0131	0.001	15.9	0
const	-0.6296	0.024	-26.3	0

[a]Number of data in clear sky days: 1341, Method: Least Squares, r^2: 0.67

Table 4. Changes of r^2 and *P*-values by dropping a variable at a time from the linear model.

Drop variable	r^2	*P value*
θs	0.45	0
φ_v	0.66	0
w_d	0.65	0
w_s	0.60	0

The results for measurements collected on non-clear sky days are also shown in Fig S5 (see Supplement 1). Since the surface-reflected light introduced to the L_t sensor is arbitrary, no obvious trends during non-clear sky days were observed.

3.4. Influence of θ_s and w_s on uncertainty

The analyses so far have shown that θ_s and w_s are the major environmental factors associated with the uncertainty in R_{rs} and nL_w. A further analysis was performed to investigate how changes of θ_s and w_s affect the uncertainty. Here we take the changes of $\mu_{nLw(\%)}$ vs. θ_s (or w_s) as examples.

3.4.1. Solar zenith angle

One of the most important factors that affects the uncertainty of nL_w is θ_s, as it directly impacts ρ (Fig. 12). If ρ is not estimated accurately, significant uncertainties in nL_w can occur, especially for near-zenith θ_s. For the cloud-free measurements during AMT28, the variation of $\mu_{nLw(\%)}$ with θ_s at different wavelengths as shown in Fig. 13. For θ_s from 10° to 20°, there was a slight decrease in uncertainty, and when $\theta_s > 40°$ there was an increase in uncertainty. At low θ_s, the uncertainty increased due to a more significant effect of sun glint, while the larger percentage uncertainty at high θ_s was likely attributed to lower signal magnitude of illumination corresponding to lower signal to noise ratios under these conditions. The pattern was more evident at 550 nm (Fig. 13(c)) as the water leaving radiance decreased significantly towards longer wavelengths in these, mostly blue, open-ocean waters. This result indicates that for an underway platform, a favorable θ_s for reduction of uncertainty appears to be at ~ 20° - 50°.

3.4.2. Wind speed

Previous studies have shown that w_s is an important factor affecting the quality of R_{rs} and nL_w from above-surface radiometric measurements [38,39]. For non-zero w_s, the wave facets reflect the incident rays in various directions. In this case, the L_t sensor can also detect reflected light from a larger portion of the sky. This effect became more significant when w_s was high (Fig. 14).

Optics EXPRESS

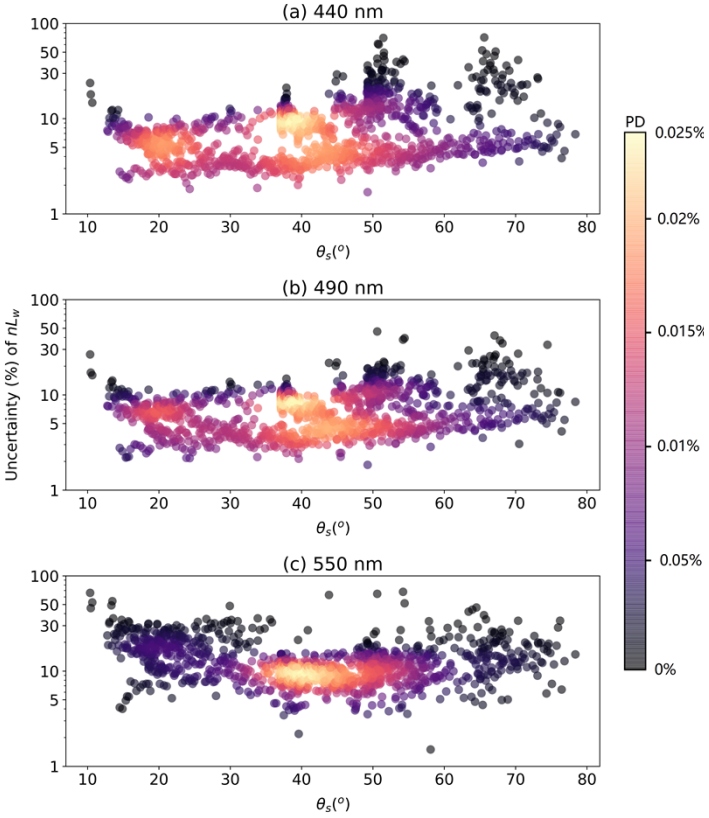

Fig. 13. Variation of percent uncertainty of nL_w with θ_s at (a) 440, (b) 490, (c) 550 nm.

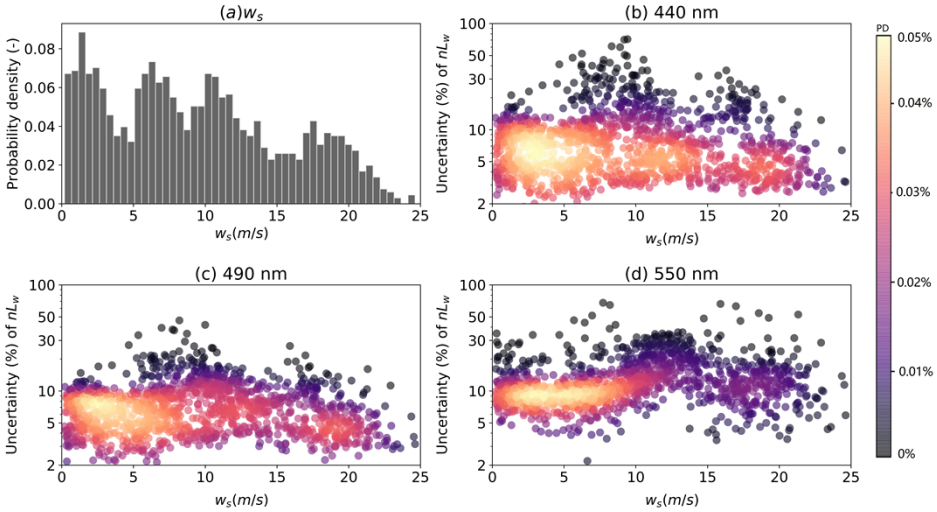

Fig. 14. (a) Histogram of wind speed, w_s, during the entire field campaign and as a percentage of variation in uncertainty for nL_w at (b) 440, (c) 490 and (d) 550 nm.

Optics EXPRESS

The distribution of w_s during cloud-free measurements, varied from 0–25 m/s with a mean value of ~10 m/s (Fig. 14(a)). The variation in uncertainty for nL_w vs. w_s at different wavelengths are shown in Fig. 14(b)-(d). The distribution of the data indicates that nL_w (or R_{rs}) derived from measurements collected at low w_s generally had lower uncertainty compared to those at high w_s conditions. The uncertainty was highest at ~ 8–15 m/s. The peak at this range was due to the data points with higher ρ especially at values > 0.1, when w_s was ~ 8–15 m/s (Fig. 12(c)) which also correspond with lower solar zenith (see Fig. 12(a), $\theta_s < 30°$ when $\rho > 0.1$) which can be related to the effect of sun glint. There were also higher uncertainties (> 15%) for $\theta_s < 30°$ (see Fig. 13(c)), which was consistent with the uncertainty > 15% at ~ 8–15 m/s shown in Fig. 14(d). Note that the measurements collected at high w_s conditions are typically excluded for satellite validation because of their high uncertainties.

4. Discussion

4.1. Comparison with other studies

A growing amount of literature has been published over the past decade on the uncertainty of radiometric measurements or derived products [16,40–44]. Each study uses a different approach to compute uncertainty ranging from repeat surveys and inter-comparisons [40], the Monte Carlo method [41], and the LPU [16,42,43].

4.1.1. Repeat surveys and inter-comparisons

More specifically, Antoine, et al. [40] assessed the uncertainty of a new above-water radiometer (DALEC) by comparing it with two in-water instruments and showed that the measurements from all systems matched well, with no bias and a dispersion of about 8% for wavelength < 600 nm. At red wavelengths, the dispersion was greater (25-50%) especially for clear oligotrophic water, however a full uncertainty budget was not computed for each instrument system. In this study, the overall uncertainty for R_{rs} varies from 2% to 20% for wavelength < 600 nm and increased by 4-fold (5 to 80%) at red wavelengths. The difference in uncertainties between the two studies is due to the different methods of accounting for uncertainty. The inter-comparison approach does not consider uncertainty associated with instrument characteristics and importantly, the variation in environmental conditions, whereas we accounted for all of these factors. The advantage of the inter-comparison approach is that it is direct and easily implemented, and was therefore adopted historically as an efficient and simple way of estimating the uncertainty of radiometric measurements [6,7,45,46]. The uncertainty estimated using the inter-comparison approach is approximate however, and with this method it is not possible to investigate the uncertainty budget associated with different sources.

4.1.2. Monte Carlo method

Monte Carlo methods are particularly useful for understanding measurement uncertainty. Białek, et al. [41] for example, used the Monte Carlo method to conduct an uncertainty analysis for in-situ radiometers using various instrument characteristics. They showed that stray light, cosine response, temperature and non-linearity corrections are particularly important to consider in the computation of uncertainty, though they did not consider environmental effects, such as waves and sun glint. By comparison, our study obtained similar results but found that the environmental variability was the most important uncertainty source (e.g., an average of > 50% contribution in the total uncertainty of L_t). In addition, the Monte Carlo approach is computationally expensive and therefore can be prohibitive or impractical to implement for continuous above-water measurements that generate large volumes of data in an efficient processing chain. There is a need to optimize data radiometric processing in a community processing chain that is commonly available for all scientists, to reduce the variation between processors (e.g. Tilstone et al. [6])

Optics EXPRESS

and to provide consistent results for the basis of FRM databases for ocean colour validation. The Monte Carlo method may not be the most optimal approach for this.

4.1.3. LPU

The use of the LPU has been advocated as the standard and accepted approach to assess the uncertainty. It is computationally efficient and can be implemented using high volumes of data. Alikas, et al. [16] used this approach for screening the highest quality radiometric measurements to validate Sentinel-3A OLCI radiometric products over optically complex Estonian lakes and the Baltic Sea. The uncertainty analysis suggested that the in-situ radiometric measurements should be performed under optimal conditions to reduce noise in the data that arise during poor environmental conditions such as high wind speed, wave height, high solar zenith angle. They also showed that the uncertainty of R_{rs} was highest in short visible bands (400 nm) and decreased toward longer wavelengths (560 nm). We observed the opposite trend in our data with increasing uncertainty from 410 to 550 nm. The difference could result from the different water types of interest for both studies. In the study of Alikas, et al. [16], optically complex inland and coastal waters were investigated while in our study we focused on comparatively optically clear open ocean waters.

Similarly, Brown, et al. [43] used the LPU to compute an uncertainty budget for MOBY based on up-welling radiance and suggested updates in the instrumentation to reduce the uncertainties in in-situ water-leaving radiance measurements are required. The study concluded that if MOBY instruments are properly maintained and calibrated, a long-term radiometric uncertainty of 3% level can be achieved. Our study using the HyperSAS above-water measurement system had higher uncertainty (average uncertainty of > 3%), due to of the higher range in environmental factors, such as sun glint and wind speed, that can be expected on a moving platform.

McKinna, et al. [42] demonstrated a first-order-first-moment (FOFM) method based on the LPU for estimating the uncertainties of ocean color products (e.g., Chl *a*, particulate organic carbon, and phytoplankton absorption and particle scattering coefficients at 440 nm). By comparison, results from the FOFM-based method with the Monte Carlo method, it showed that there was good agreement in the uncertainties computed using both methods, with a mean difference of < 3%, when used to validate NASA ocean color products.

4.1.4. Assessment of uncertainty using the LPU

In this study, we focused on the uncertainty budget for continuous HyperSAS measurements using the LPU. The instruments were calibrated before and after the campaign and the characterization of the radiometers was conducted after the campaign. By analyzing the distribution of uncertainties, we were able to investigate the major uncertainty sources and environmental factors that impact uncertainty most. From these, recommendations are proposed to improve data quality of radiometric measurements (see section 4.6).

4.2. Uncertainty from temperature characterization

4.2.1. Temperature correction coefficients

Zibordi, et al. [23] investigated the effects of temperature on radiometric measurements from TriOS-RAMSES sensors and showed that the difference of measurements at ambient temperatures (10 °C – 40 °C) with respect to reference values at 20 °C can be up to 5% for wavelengths between 400 and 800 nm. The effects generally increased with increasing wavelength and were highest in the near-infrared. In their study, the mean temperature coefficients varied from -0.04 × 10^{-2} $°C^{-1}$ at 400nm to 0.33 × 10^{-2} $°C^{-1}$ at 800nm. Similarly, in our study we also determined the variation in correction coefficients due to temperature for each of the three radiometers that comprise the radiometer measurement system following Vabson, et al. [20]. In our study, the mean temperature coefficients varied from -0.15 × 10^{-2} $°C^{-1}$ to 0.2 × 10^{-2} $°C^{-1}$ over the same

Optics EXPRESS

wavelength range (400–800 nm) and were therefore slightly lower compared to those reported by Zibordi, et al. [23] and illustrate the differences between Seabird HyperSAS and TriOS-RAMSES measurement systems.

4.2.2. Uncertainty from temperature correction

We found that the mean uncertainty from temperature correction coefficients is 0.02×10^{-2} °C^{-1} for 400–800 nm, which is close to that reported by Zibordi, et al. [23] (0.03×10^{-2} °C^{-1}). The final contribution to uncertainty by the temperature correction is small and < 1% (Fig. 11, S4). By comparison, when the temperature correction coefficients of Zibordi, et al. [23] were applied to our measurements, the overall mean uncertainty of nL_w were still less than 1%, since the uncertainty from temperature correction only contributes a very small amount to the uncertainty budget.

4.3. Uncertainty associated with stray light

Talone, et al. [31] found that for Level 1 radiometer data (i.e., radiance or irradiance), stray light generally contributes < 1% of the measured signal. A mean uncertainty of 0.25% for E_s and L_i and 0.5% for $L_t$were applied [31]. Similarly, Habauzit, et al. [47] developed a simple algorithm based on a combination of two calibration techniques to correct for stray light effects and computed an uncertainty in the correction algorithm of 0.5%. This straylight correction approach was also used for the MOBY system [48].

In this study, the correction algorithm of Zong, et al. [22] was applied to all radiometric measurements. The correction uncertainty was considered as Type B uncertainty evaluation (Table 1) and for individual parameters (e.g. L_t) the contribution by straylight correction to the total uncertainty was small (~ 1%). The uncertainty computed from stray light correction is dependent on the algorithms applied and differs for each radiometer. The impact of different correction algorithms for stray light to the overall uncertainty has not so far been assessed in the current available literature. Further investigation into the best and most appropriate method for reducing the uncertainty would therefore be beneficial.

4.4. Uncertainty from non-linearity correction

The non-linearity effect for optical radiometers cannot be neglected. Vabson, et al. [30] reported that the maximum relative difference between spectra due to non-linearity could be greater than 1.5%. By comparison, for non-linearity effects on multiple radiometers, they also found that variability between radiometers due to this effect if not corrected is ± 1%, but the differences between measurement spectra after the non-linearity correction was < 0.2%. In this study, the non-linearity correction coefficients were determined in the laboratory in the same way as Vabson, et al. [30], and the mean value (α) was between -1×10^{-8} DN^{-1} and -2×10^{-6} DN^{-1} for 400–800 nm with the mean uncertainty of -4.5×10^{-8} DN^{-1}. For the overall uncertainty of Level 1 data (e.g., L_t), the uncertainty contribution propagated from α was small (< 1%). By comparison, we applied the nonlinear correction coefficients of Vabson, et al. [30] to our measurements. It showed that the change of uncertainty budget can be ignored (< 0.1%) because of very small uncertainty contribution associated with nonlinear correction. It is worth noting that non-linearity characterization can be well determined in the Laboratory, but some extra uncertainty could be introduced when unstable natural radiation sources are measured.

4.5. Uncertainty from environmental factors

Environmental factors have a big impact on the uncertainty of above water measurements. In the study of Alikas, et al. [16], a PCA analysis on field measurements showed that, among the environmental factors considered, which included wave height, wind speed, sky conditions, the solar zenith angle contributed most to the uncertainty, especially when phytoplankton biomass

Optics EXPRESS

was high. Similarly, the studies of Zibordi, et al. [9] indicated that environmental factors contributed most to the uncertainty and of these, wave effects and changes in the optical properties of seawater during the measurement sequence, contributed the most. On AMT28, a more detailed investigation showed that illumination conditions (i.e., sky cloudiness), solar position and wind speed are the most important environmental factors affecting the uncertainty of above water measurements.

For effects of sky conditions, the overall uncertainties were generally lower for clear-sky measurements compared to cloudy-sky measurements. These are mainly due to smaller variation in L_i and L_t under clear sky over the time span of measurements, if the effect of sun glint is minimal. It is worth noting that for scattered clouds and partially obscured sun conditions, the illumination conditions could change very fast, which can produce large deviations in L_i. For L_t, the contributions to surface-reflected radiance arise from different portions of the sky and can be arbitrary because of temporal variations associated with surface waves, which could result in high uncertainty of L_t.

Wind is an important environmental factor impacting the estimation of R_{rs} or nL_w. To remove skylight from L_t, Mobley [38] provided a lookup table for ρ as a function of wind speed assuming a Cox-Munk relationship [49] between surface field and wind speed. It shows that the value of ρ generally increases with wind speed for clear sky conditions. In this study, we obtained a similar trend with ρ increasing from ~ 0.03 to ~0.2 when the wind speed increased from 0 to 25 m/s. The uncertainty is also highly related to wind speed and generally increases with wind speed (Fig. 12(c), 14). From the measurements collected on AMT28, the favorable condition for above-water measurements with low uncertainty are at wind speeds of < ~ 7 m/s, which is consistent with the results of Mobley [38]. During the AMT cruise, the mean wind speed for clear sky conditions was 9 m/s with ~30% measurements collected at low wind speed (< 5 m/s).

In addition, it appears that smaller uncertainty can be achieved at θ_s in the range of ~ 20° - 50° and large uncertainty could be introduced for the sun at zenith. This could be attributed to the impact of sun glint on L_t. Using underway measurement systems with small θ_s, it is difficult to obtain an optimal viewing geometry to avoid sun glint as the directionality of sun glint is ambiguous and unpredictable because of surface waves. For the continuous measurements made on AMT28, the sensor azimuth viewing angle (φ_v) varied over a wide range from ~50° to 160°, which differed from the recommended optimal azimuth angle ($\varphi_v = 140°$). This can result in high uncertainty at low θ_s (< 20°).

There are also other environmental factors that affect the uncertainty, such as surface wave perturbations, self-shading from the ship and variability of water inherent optical properties. These factors also need to be taken into account to have confidence in the in-situ data especially when used to validate ocean color products.

4.6. Recommendations

The continuous radiometric measurements made on an Atlantic Meridional Transect enabled us to investigate the main sources of uncertainty and therefore to improve the quality of the data collected. For a comprehensive analysis of these, it is recommended that prior to computing uncertainty that the specific and individual radiometers are properly characterized for non-linearity, straylight, temperature, rather than using generic class specific radiometer characteristics. This knowledge is critical for correcting the impacts of uncertainty, especially stray light, non-linearity and temperature on R_{rs} or nL_w and also provides a guide as to how the uncertainty can be reduced. Since the characterization of different radiometers could vary, it is essential to determine their characterization independently. The calibration and characterization of the radiometers can drift over time. Post-cruise calibration and characterization are therefore also highly recommended. For measurement conditions, it is suggested that in-situ radiometric measurements are made under the following optimal conditions: clear skies (no impact from clouds or 100% cloudless),

Optics EXPRESS

low wind speeds (< ~ 7 m/s), appropriate solar zenith angle (~ 20° - 50°) and optimal viewing geometry for minimal effect of sun glint.

5. Summary

This study developed a practical methodology for estimating uncertainty budgets for continuous above-water radiometric measurements. The average percentage uncertainty for R_{rs} over an Atlantic Meridional Transect was ~ 10% for wavelengths < 490 nm and ~ 15% for wavelengths > 550 nm. Reduced average uncertainty was found for clear sky days (~ 6% for wavelengths < 490 nm and ~ 12% for wavelengths > 550nm). The most important source of uncertainty was the environmental variability. The impacts of skylight condition, solar zenith angle and wind speed on R_{rs} showed that uncertainties were lower under clear-sky conditions, at low-wind speeds and for appropriate solar zenith (~ 20° - 50°) especially at long wavelengths. This work demonstrates that it is possible to collect measurements using continuous ship-borne radiometers that can meet the accuracy requirement of fiducial reference measurements for satellite ocean colour validation.

Funding. UK Natural Environment Research Council (NERC) National Capability funding to Plymouth Marine Laboratory for the Atlantic Meridional Transect (NE/R015953/1); UK Research and Innovation Future Leader Fellowship (MR/V022792/1); National Centre for Earth Observation (NCEO); European Commission Horizon 2020 project Copernicus Evolution - Research for Transitional-water Observation (CERTO, grant number 870349); European Space Agency grants; AMT4SentinelFRM (ESRIN/RFQ/3-14457/16/I-BG), and AMT4OceanSatFlux (4000125730/18/NL/FF/gp) and (AMT4CO2Flux 4000136286/21/NL/FF/ab).

Acknowledgments. The authors would like to thank the captain and crew of RRS James Clark Ross on AMT28.

Disclosures. The authors declare no conflicts of interest.

Data Availability. Data underlying the results presented in this paper are not publicly available at this time but may be obtained from the authors upon reasonable request.

Supplemental document. See Supplement 1 for supporting content.

References

1. A. Morel and S. Maritorena, "Bio-optical properties of oceanic waters: A reappraisal," J. Geophys. Res.: Oceans **106**(C4), 7163–7180 (2001).
2. R. Austin and T. J. Petzold, "The determination of the diffuse attenuation coefficient of sea water using the Coastal Zone Color Scanner," in *Oceanography from space* (Springer, 1981), pp. 239–256.
3. R. Frouin, J. McPherson, K. Ueyoshi, and B. A. Franz, "A time series of photosynthetically available radiation at the ocean surface from SeaWiFS and MODIS data," in *Remote Sensing of the Marine Environment II*, (International Society for Optics and Photonics, 2012), 852519.
4. G. Zibordi, C. J. Donlon, and A. C. Parr, *Optical radiometry for ocean climate measurements* (Academic Press, 2014).
5. S. B. Hooker, G. Lazin, G. Zibordi, and S. McLean, "An evaluation of above-and in-water methods for determining water-leaving radiances," J. Atmos. Oceanic Technol. **19**(4), 486–515 (2002).
6. G. Tilstone, G. Dall'Olmo, M. Hieronymi, K. Ruddick, M. Beck, M. Ligi, M. Costa, D. D'alimonte, V. Vellucci, and D. Vansteenwegen, "Field intercomparison of radiometer measurements for ocean colour validation," Remote Sens. **12**(10), 1587 (2020).
7. G. Zibordi, K. Ruddick, I. Ansko, G. Moore, S. Kratzer, J. Icely, and A. Reinart, "In situ determination of the remote sensing reflectance: an inter-comparison," Ocean Sci. **8**(4), 567–586 (2012).
8. G. Zibordi, B. N. Holben, M. Talone, D. D'Alimonte, I. Slutsker, D. M. Giles, M. G. J. J. o, A. Sorokin, and O. Technology, "Advances in the ocean color component of the Aerosol Robotic Network (AERONET-OC)," 38(4), 725–746 (2021).
9. G. Zibordi, F. Mélin, J.-F. Berthon, B. Holben, I. Slutsker, D. Giles, D. D'Alimonte, D. Vandemark, H. Feng, and G. Schuster, "AERONET-OC: a network for the validation of ocean color primary products," Journal of Atmospheric Oceanic Technology **26**(8), 1634–1651 (2009).
10. V. E. Brando, J. L. Lovell, E. A. King, D. Boadle, R. Scott, and T. Schroeder, "The potential of autonomous ship-borne hyperspectral radiometers for the validation of ocean color radiometry data," Remote Sensing **8**(2), 150 (2016).
11. R. J. Brewin, G. Dall'Olmo, S. Pardo, V. van Dongen-Vogels, and E. Boss, "Underway spectrophotometry along the Atlantic Meridional Transect reveals high performance in satellite chlorophyll retrievals," Remote Sens. Environ. **183**, 82–97 (2016).
12. P. Qin, S. G. Simis, and G. H. Tilstone, "Radiometric validation of atmospheric correction for MERIS in the Baltic Sea based on continuous observations from ships and AERONET-OC," Remote Sens. Environ. **200**, 263–280 (2017).

Optics EXPRESS

13. S. G. Simis and J. Olsson, "Unattended processing of shipborne hyperspectral reflectance measurements," Remote Sens. Environ. **135**, 202–212 (2013).
14. G. H. Tilstone, S. Pardo, G. Dall'Olmo, R. J. Brewin, F. Nencioli, D. Dessailly, E. Kwiatkowska, T. Casal, and C. Donlon, "Performance of Ocean Colour Chlorophyll a algorithms for Sentinel-3 OLCI, MODIS-Aqua and Suomi-VIIRS in open-ocean waters of the Atlantic," Remote Sens. Environ. **260**, 112444 (2021).
15. J. L. Mueller, A. Morel, R. Frouin, C. Davis, R. Arnone, K. Carder, Z. Lee, R. Steward, S. Hooker, and C. Mobley, "*Ocean Optics Protocols For Satellite Ocean Color Sensor Validation, Revision 4. Volume III: Radiometric Measurements and Data Analysis Protocols*," Ocean Best Practices (2003).
16. K. Alikas, I. Ansko, V. Vabson, A. Ansper, K. Kangro, K. Uudeberg, and M. Ligi, "Consistency of Radiometric Satellite Data over Lakes and Coastal Waters with Local Field Measurements," Remote Sensing **12**(4), 616 (2020).
17. I. Iso, "Guide to the Expression of Uncertainty in Measurement," Joint Committee for Guides in Metrology–JCGM 100. 2008 (ISO/IEC Guide 98–3) http://www.iso.org/sites/JCGM/GUM-introduction.htm(2008).
18. L. Kirkup and R. B. Frenkel, *An introduction to uncertainty in measurement: using the GUM (guide to the expression of uncertainty in measurement)* (Cambridge University Press, 2006).
19. I. Ansko, J. Kuusk, R. Vendt, and V. Vabson, "MERIS Validation and Algorithm 4th reprocessing–MERIS Validation Team (MVT)," Tartu Observatory, Tõravere, INTERMEDIATE REPORT (2015).
20. V. Vabson, J. Kuusk, I. Ansko, R. Vendt, K. Alikas, K. Ruddick, A. Ansper, M. Bresciani, H. Burmester, and M. Costa, "Laboratory intercomparison of radiometers used for satellite validation in the 400–900 nm range," Remote Sensing **11**(9), 1101 (2019).
21. G. Zibordi, K. Voss, B. Johnson, and J. J. I. P. D. Mueller, "Protocols for satellite ocean color data validation: in situ optical radiometry," (2014).
22. Y. Zong, S. W. Brown, G. Meister, R. A. Barnes, and K. R. Lykke, "Characterization and correction of stray light in optical instruments," Proc. SPIE **67441**, 67441L (2007).
23. G. Zibordi, M. Talone, and L. Jankowski, "Response to Temperature of a Class of In Situ Hyperspectral Radiometers," Journal of Atmospheric Oceanic Technology **34**(8), 1795–1805 (2017).
24. G. Zibordi, K. J. Voss, B. C. Johnson, and J. L. Mueller, "Protocols for Satellite Ocean Colour Data Validation: In Situ Optical Radiometry," IOCCG Protocol Series (2019).
25. A. Morel, D. Antoine, and B. Gentili, "Bidirectional reflectance of oceanic waters: accounting for Raman emission and varying particle scattering phase function," Appl. Opt. **41**(30), 6289–6306 (2002).
26. J. E. O'Reilly, S. Maritorena, D. A. Siegel, M. C. O'Brien, D. Toole, B. G. Mitchell, M. Kahru, F. P. Chavez, P. Strutton, and G. F. Cota, "Ocean color chlorophyll a algorithms for SeaWiFS, OC2, and OC4: Version 4," SeaWiFS postlaunch calibration validation analyses **3**, 9–23 (2000).
27. G. Thuillier, M. Hersé, T. Foujols, W. Peetermans, D. Gillotay, P. Simon, and H. Mandel, "The solar spectral irradiance from 200 to 2400 nm as measured by the SOLSPEC spectrometer from the ATLAS and EURECA missions," Sol. Phys. **214**(1), 1–22 (2003).
28. J. Mueller, C. Pietras, S. Hooker, R. Austin, M. Miller, K. Knobelspiesse, R. Frouin, B. Holben, and K. Voss, "Ocean Optics Protocols For Satellite Ocean Color Sensor Validation, Revision 4. Volume II: Instrument Specifications, Characterization and Calibration," (2003).
29. J. C. Damasceno and P. R. Couto, "Methods for evaluation of measurement uncertainty," in *Metrology* (IntechOpen London, 2018), pp. 9–28.
30. V. Vabson, J. Kuusk, I. Ansko, R. Vendt, K. Alikas, K. Ruddick, A. Ansper, M. Bresciani, H. Burmester, and M. Costa, "Field intercomparison of radiometers used for satellite validation in the 400–900 nm range," Remote Sens. **11**(9), 1129 (2019).
31. M. Talone, G. Zibordi, I. Ansko, A. C. Banks, and J. Kuusk, "Stray light effects in above-water remote-sensing reflectance from hyperspectral radiometers," Appl. Opt. **55**(15), 3966–3977 (2016).
32. M. Talone and G. Zibordi, "Polarimetric characteristics of a class of hyperspectral radiometers," Appl. Opt. **55**(35), 10092–10104 (2016).
33. M. Talone, G. Zibordi, and Z. Lee, "Correction for the non-nadir viewing geometry of AERONET-OC above water radiometry data: an estimate of uncertainties," Opt. Express **26**(10), A541–A561 (2018).
34. K. G. Ruddick, K. Voss, E. Boss, A. Castagna, R. Frouin, A. Gilerson, M. Hieronymi, B. C. Johnson, J. Kuusk, and Z. Lee, "A review of protocols for fiducial reference measurements of water-leaving radiance for validation of satellite remote-sensing data over water," Remote Sens. Environ. **11**(19), 2198 (2019).
35. M. J. Reno and C. W. Hansen, "Identification of periods of clear sky irradiance in time series of GHI measurements," Renewable Energy **90**, 520–531 (2016).
36. W. W. Gregg and K. L. Carder, "A simple spectral solar irradiance model for cloudless maritime atmospheres," Limnol. Oceanogr. **35**(8), 1657–1675 (1990).
37. J. Wei, Z. Lee, and S. Shang, "A system to measure the data quality of spectral remote-sensing reflectance of aquatic environments," J. Geophys. Res.: Oceans **121**, 8189–8207 (2016).
38. C. D. Mobley, "Estimation of the remote-sensing reflectance from above-surface measurements," Appl. Opt. **38**(36), 7442–7455 (1999).
39. J. L. Mueller, C. Davis, R. Arnone, R. Frouin, K. Carder, Z. Lee, R. Steward, S. Hooker, C. D. Mobley, and S. McLean, "Above-water radiance and Remote Sens. Environ. reflectance measurements and analysis protocols," Ocean Optics protocols for satellite ocean color sensor validation Revision **2**, 98–107 (2000).

Optics EXPRESS

40. D. Antoine, M. Slivkoff, W. Klonowski, C. Kovach, and M. Ondrusek, "Uncertainty assessment of unattended above-water radiometric data collection from research vessels with the Dynamic Above-water Radiance (L) and Irradiance (E) Collector (DALEC)," Opt. Express **29**(3), 4607–4631 (2021).
41. A. Białek, S. Douglas, J. Kuusk, I. Ansko, V. Vabson, R. Vendt, and T. Casal, "Example of Monte Carlo Method Uncertainty Evaluation for Above-Water Ocean Colour Radiometry," Remote Sens. **12**(5), 780 (2020).
42. L. I. McKinna, I. Cetinić, A. P. Chase, and P. J. Werdell, "Approach for propagating radiometric data uncertainties through NASA ocean color algorithms," Front. Earth Sci. **7**, 176 (2019).
43. S. W. Brown, S. J. Flora, M. E. Feinholz, M. A. Yarbrough, T. Houlihan, D. Peters, Y. S. Kim, J. L. Mueller, B. C. Johnson, and D. K. Clark, "The Marine Optical BuoY (MOBY) radiometric calibration and uncertainty budget for ocean color satellite sensor vicarious calibration," in *Sensors, Systems, and Next-Generation Satellites XI*, (International Society for Optics and Photonics, 2007), 67441 M.
44. G. Zibordi, F. Mélin, K. J. Voss, B. C. Johnson, B. A. Franz, E. Kwiatkowska, J.-P. Huot, M. Wang, and D. Antoine, "System vicarious calibration for ocean color climate change applications: Requirements for in situ data," Remote Sens. Environ. **159**, 361–369 (2015).
45. M. Ondrusek, V. P. Lance, M. Wang, R. A. Arnone, S. Ladner, W. Goode, R. Vandermeulen, S. Freeman, J. E. Chaves, and A. Mannino, "Report for dedicated JPSS VIIRS ocean color December 2015 calibration/validation cruise," (2016).
46. A. Hommersom, S. Kratzer, M. Laanen, I. Ansko, M. Ligi, M. Bresciani, C. Giardino, J. M. Beltrán-Abaunza, G. Moore, and M. R. Wernand, "Intercomparison in the field between the new WISP-3 and other radiometers (TriOS Ramses, ASD FieldSpec, and TACCS)," J. Appl. Remote Sens **6**(1), 063615 (2012).
47. C. Habauzit, S. W. Brown, K. R. Lykke, B. C. Johnson, M. E. Feinholz, M. Yarbrough, D. K. J. J. o, A. Clark, and O. Technology, "Radiometric characterization and absolute calibration of the Marine Optical System (MOS) bench unit," 20, 383–391 (2003).
48. D. K. Clark, M. Feinholz, M. Yarbrough, B. C. Johnson, S. W. Brown, Y. S. Kim, and R. A. Barnes, "Overview of the radiometric calibration of MOBY," in *Earth Observing Systems VI*, (International Society for Optics and Photonics, 2002), 64–76.
49. C. Cox and W. Munk, "Measurement of the roughness of the sea surface from photographs of the sun's glitter," J. Opt. Soc. Am. **44**(11), 838–850 (1954).